Characterizing the local vectorial electric field near an atom chip using Rydberg-state spectroscopy

N. Cisternas,[*] Julius de Hond, G. Lochead,[†] R. J. C. Spreeuw, H. B. van Linden van den Heuvell, and N. J. van Druten
Van der Waals-Zeeman Institute, Institute of Physics, University of Amsterdam, Amsterdam, Netherlands
(Received 19 May 2017; published 25 July 2017)

We use the sensitive response to electric fields of Rydberg atoms to characterize all three vector components of the local electric field close to an atom-chip surface. We measured Stark-Zeeman maps of S and D Rydberg states using an elongated cloud of ultracold rubidium atoms (temperature $T \sim 2.5$ μK) trapped magnetically 100 μm from the chip surface. The spectroscopy of S states yields a calibration for the generated local electric field at the position of the atoms. The values for different components of the field are extracted from the more complex response of D states to the combined electric and magnetic fields. From the analysis we find residual fields in the two uncompensated directions of 0.0 ± 0.2 and 1.98 ± 0.09 V/cm. This method also allows us to extract a value for the relevant field gradient along the long axis of the cloud. The manipulation of electric fields and the magnetic trapping are both done using on-chip wires, making this setup a promising candidate to observe Rydberg-mediated interactions on a chip.

DOI: 10.1103/PhysRevA.96.013425

I. INTRODUCTION

An important challenge in the implementation of quantum information protocols and in quantum simulation is to create strong, long-range, tunable, and switchable interactions. Rydberg atoms have exaggerated properties, such as very large electrical polarizabilities and (induced) dipole moments [1]. These characteristics make them very good candidates as mediators of the needed interactions and are the reason why they are now being widely pursued as systems for quantum information science using various approaches, including cavity quantum electrodynamics [2], trapped ions [3], and neutral atoms [4–6]. Among these approaches the combination of atom chips with neutral atoms offers unique opportunities to study quantum-degenerate gases [7] with the advantage of having a compact system that allows the efficient manipulation of quantum gases. Due to their sensitive response to electric fields, Rydberg atoms are also used as a tool for electrometry [8]. One of the disadvantages of using Rydberg atoms in an atom-chip experiment is the presence of spatially inhomogeneous electric fields [9–11]. These fields are produced, e.g., by adsorbates (deposited) on the surface of the chip [10–12] or by a voltage drop across current-carrying wires on the chip. Due to the large polarizability of Rydberg atoms and their proximity to a surface, the coherence of the excitation will be limited by these stray electric fields. This makes the observation of Rydberg-mediated interactions in such systems a challenge. A detailed characterization of the mentioned stray electric fields is therefore crucial.

Here, we employ two-photon Rydberg Stark-Zeeman spectroscopy of a cloud of magnetically trapped ultracold ^{87}Rb atoms (temperature $T \sim 2.5$ μK) to characterize the local electric fields from an atom-chip surface ($\sim$100 μm distance). An additional auxiliary electric field is generated at the location of the atoms by applying a voltage to an on-chip wire adjacent to the magnetic trapping wire. We show that it is possible to characterize the two uncompensated vector components of the local electric field (the third component is compensated by the auxiliary electric field) by a careful analysis of the measured Stark-Zeeman spectra of S and D states. The results are consistent with the calculated structure of Rydberg states in combined magnetic and electric fields. We also characterize the electric field gradient along the long axis of the cloud.

This paper is structured as follows. In Sec. II we summarize our calculations of D-state Stark-Zeeman maps for different field configurations and show how these are affected by residual fields in different directions. The experimental setup and data acquisition procedure are explained in Sec. III, followed by the main experimental results and a comparison with the calculations described in the previous section. A summary of the main results is given in Sec. IV.

II. STARK MAP SIMULATIONS

To compare our experimental results to theory, we need to calculate the Rydberg energies and eigenstates in combined electric and magnetic fields, with an *a priori* unknown angle between the two. To this end, we first calculate field-free radial Rydberg wave functions, then include the electric field by calculating the matrix elements of the electric-field operator and diagonalizing the result to obtain Stark eigenstates and eigenenergies, and, finally, take into account the magnetic field as a small perturbation in the Hamiltonian to obtain combined Stark-Zeeman maps. We have verified that the results of our calculations are consistent with results from open-source Rydberg calculator packages [13,14] that have recently become available.

In more detail, the calculation of the desired Stark-Zeeman maps starts from the binding energies $E_b = -R/[2(n-\delta)^2]$ of the field-free Rydberg states, given by the experimentally determined quantum defects $\delta_{n,l,j}$ of ^{87}Rb for S and D states [15], P states [16], F states [17], and G states [18] and the reduced Rydberg constant R for ^{87}Rb. Here, n is the principal quantum number, l is the orbital angular momentum, and j is the total angular momentum of the valence electron. For $l > 4$ the quantum defect is negligibly small, and we set it to zero. Under field-free conditions, the Rydberg wave

[*]n.v.cisternassanmartin@uva.nl
[†]Present address: Physikalisches Institut, Universitat Heidelberg, Heidelberg, Germany.

functions separate into a product of a radial wave function and a remaining function describing the electron spin and angular part of the wave function. The radial wave functions $\psi_{n,l,j}(r)$ are obtained numerically using the Numerov method [19,20], integrating the radial Schrödinger equation inward starting from the classically forbidden outer region of the Coulomb potential with an energy given by the above quantum defects and with a variable step size adapted to the changing spatial oscillation frequency of the wave function [21]. The spin and angular functions are obtained from the standard angular momentum algebra using the Wigner-Eckart theorem [22]. In an applied electric field, m_j (corresponding to the projection of the angular momentum onto the electric-field direction) remains a good quantum number. The energies and eigenstates depend on m_j and can be obtained for each m_j separately. To this end, a set of all states with energies around the energy of interest is selected (typically ∼1000 states) for each m_j, and a finite-size matrix is set up with the diagonal elements given by the (field-free) energies and the off-diagonal elements given by the matrix elements of the electric-field operator. The latter are obtained using the above radial wave functions for the radial matrix elements and the Clebsch-Gordan coefficients for the angular part. The resulting matrix is diagonalized, yielding a Rydberg Stark map of energies and eigenvectors for each m_j as a function of electric-field strength E.

To account for magnetic fields of a few gauss, we limit ourselves to a single value for n, l, and j (consistent with our magnetic trap) and the corresponding set of $(2j+1)$ basis states distinguished by their value of m_j (with the quantization axis along the electric-field direction). The corresponding eigenenergies $E(n,l,j,m_j)$ yield a (diagonal) Stark Hamiltonian matrix within this manifold. Within this basis set the Zeeman Hamiltonian (with the magnetic field at an angle with respect to the electric field) is added as a perturbation, and the resulting matrix is again diagonalized to yield a Stark-Zeeman map of eigenvalues and eigenstates. This method works well as long as the Zeeman splittings are much below the fine-structure splitting (this is 560 MHz for the $28D$ state, so that the magnetic field should be below 100 G). The results of such a calculation are shown in Fig. 1.

From these calculations it is possible to analyze the character of each sublevel after a projection of the eigenbasis on the B field direction. At zero electric field each sublevel is defined by the Zeeman shift. In Fig. 1(a) this means that each curve represents $m_j = 5/2, 3/2, 1/2, -1/2, -3/2, -5/2$ from top to bottom, respectively. In the case in which $\vec{E} \parallel \vec{B}$ [black curves in Fig. 1(a)] the analysis is trivial because the quantization axis is unambiguous; hence, each sublevel maintains its own original character at any electric-field value. As a result the Stark shift (which depends only on the absolute value $|m_j|$) and Zeeman shift are simply additive.

The analysis is more complicated for the case when $\vec{E} \perp \vec{B}$. As the electric field is increased, the character of each state changes; for instance, the highest-energy state, $m_j = 5/2$ (along $\vec{B}$) changes its character to a superposition of $m_j = -1/2$ and $m_j = +1/2$ (along $\vec{E}$) at higher electric fields. The behavior at high electric fields can be intuitively understood as follows (we take the quantization axis along the electric field in the remainder of this paragraph). In the absence of a magnetic field the highest-energy level is twofold degenerate, with quantum numbers $m_j = \pm 1/2$. The other states, with larger $|m_j|$, are Stark shifted relatively far away (down) in energy. A small magnetic field orthogonal to the electric field couples electric-field eigenstates with $\Delta m_j = \pm 1$. This coupling is most effective between the two states with $|m_j| = 1/2$ (since these have $\Delta m_j = \pm 1$ and are degenerate in energy in the absence of a magnetic field). It splits up the upper two states into the symmetric and antisymmetric combinations of $m_j = -1/2$ and $m_j = +1/2$. The downshifted states, with larger $|m_j|$, are only weakly affected by the magnetic field (since the magnetic field does not couple within the pair with the same $|m_j| > 1/2$), and as a result for each $|m_j| > 1/2$ the two states are nearly degenerate in energy. This analysis is

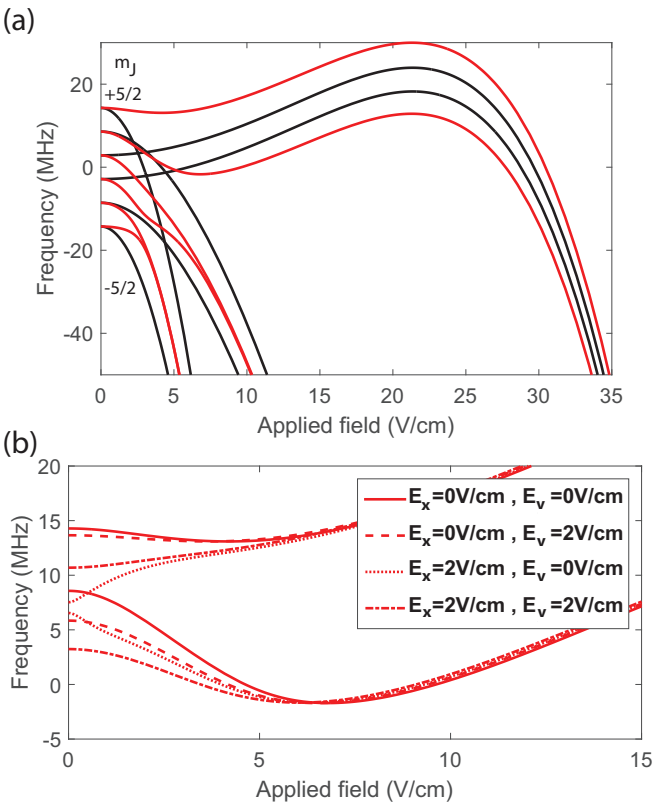

FIG. 1. (a) Calculated Stark map of the $28D_{5/2}$ state of ^{87}Rb in a magnetic field of $B = 3.4$ G. The red and black lines correspond to the cases when the magnetic field is perpendicular and parallel to the electric field, respectively. At zero electric field each line represents the sublevel $m_j = 5/2, 3/2, 1/2, -1/2, -3/2, -5/2$ from top to bottom, respectively. In the $\vec{E} \perp \vec{B}$ configuration, for the two uppermost states the initial downshift is followed by an increase in energy, thus creating an initial dip in the Stark map. This is an additional feature compared to the $\vec{E} \parallel \vec{B}$ case, and it can be used to extract information on different electric-field components. (b) Detail of the shift of the two uppermost sublevels for various stray field configurations in the case where the applied electric field $\vec{E}_{ap} \perp \vec{B}$. Here, we use an orthogonal coordinate system (x,u,v) with x along the direction of the magnetic field and u along the direction of the applied electric field $\vec{E}_{ap}$; v is perpendicular to both x and u (see Fig. 2 for a graphic description of the experimental field directions). The plot illustrates the sensitivity of the Stark-Zeeman map to different field configurations; see text for details.

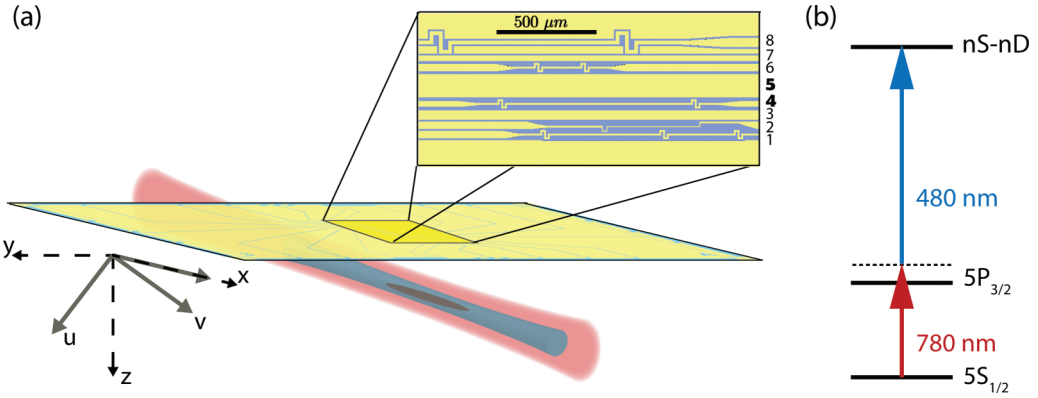

FIG. 2. (a) Sketch of the experimental geometry: We excite ^{87}Rb atoms to a Rydberg level using a two-photon excitation scheme with two counterpropagating 780- and 480-nm lasers. The atoms are magnetically trapped in vacuum ~100 μm below the surface of an atom chip. The numbering of the on-chip wires is indicated in the inset. The excitation is done along the axial direction of the cloud during magnetic trapping. The gray arrows indicate a coordinate system composed of different field components; both (x,y,z) and (x,u,v) are orthogonal systems. Namely, we call the stray electric field along the long direction of the cloud the parallel component E_x (along the direction of the x axis). We apply a voltage to wire 4 that changes the field (E_{ap} along the direction of the u axis) at the position of the atoms so we can generate Stark maps. The produced field is perpendicular to the B field and lies in the yz plane. The stray field in the third direction, labeled E_v (along the direction of the v axis), is in the yz plane and orthogonal to E_u. (b) Laser scheme for the Rydberg excitation. The intermediate state detuning from the $5P_{3/2}$ state is 100 MHz towards the blue.

important when setting the polarization of our lasers for the Rydberg excitation in order to select which state we excite in view of the selection rules. For the sake of simplicity we will use the zero-electric-field labeling (ZEL) to identify the various sublevels throughout this paper, even when the electric field has a nonzero value.

From Fig. 1(a), we see that in the case of perpendicular fields (red lines), $\vec{E} \perp \vec{B}$, the energy of the two uppermost magnetic sublevels first decreases, followed by an increase in energy at higher fields, thus creating a dip in the Stark map. The size of this initial dip is very sensitive to additional (stray) electric fields. In Fig. 1(b) we illustrate this by showing four different configurations in which we varied the contributions of residual fields between 0 and 2 V/cm. These contributions were taken parallel to the magnetic field (E_x) and perpendicular to both the applied electric field and magnetic field (E_v); a sketch of the field geometry is shown in Fig. 2(a). A stray field in the x direction of 2 V/cm already shows a total disappearance of the local minimum for the top state. More generally, the precise shape of the Stark-Zeeman map of the top two states is very sensitive to the strength of the electric-field components E_x and E_v, enabling the characterization of these fields. The role of the magnetic field is relevant because its value defines the energy difference between each magnetic sublevel at zero electric field, which is the Zeeman shift. Moreover, Fig. 1(b) shows that this energy difference varies as the electric field is increased, revealing the importance of the magnetic-field configuration in the analysis of the data. Consequently, the combination of electric and magnetic fields is crucial for the full characterization of residual unknown stray electric fields.

III. EXPERIMENTAL RESULTS

The experimental setup employs an atom chip [7] to trap and cool a cloud of Rb atoms in vacuum at a distance of ~100 μm from a set of microfabricated gold wires [see Fig. 2(a)]. Our setup and methods have been described in detail elsewhere [23–25]. In brief, we start from a cloud of ^{87}Rb atoms loaded in a mirror-magneto-optical trap (MMOT) with the mirror formed by the atom chip, a patterned 2-μm-thick gold layer on a 16×25 mm^2 silicon substrate. These atoms are then optically pumped to the $|F = 2, m_F = 2\rangle$ state and transferred to a magnetic trap where they are cooled down to ~2.5 μK using rf-induced evaporative cooling. The magnetic trapping is done using a 125-μm-wide on-chip Z-shaped wire [wire labeled 5 in Fig. 2(a)] carrying a current of 1 A. This final trap is elongated (cigar shaped), with trap frequencies $\omega_x/2\pi = 46$ Hz and $\omega_{y,z}/2\pi = 860$ Hz. The bottom of the trap is at $B = 3.41$ G (corresponding to an rf frequency of 2.39 MHz). After evaporation there are approximately 10^4 atoms in the trap. At $T = 2.5$ μK the calculated cloud size (FWHM) is 6.8 μm in the radial directions and 127 μm in the longitudinal direction. The temperature of the cloud is extracted from a time-of-flight (TOF) measurement in which the expansion of the cloud is measured as a function of the time after it was released.

This setup has been extended with a two-photon Rydberg excitation scheme. We excite atoms from the $5S_{1/2}$ ground state to a Rydberg level via the intermediate state $5P_{3/2}$ using a 780-nm infrared laser and a 480-nm blue laser in a 7-ms pulse during magnetic trapping. Both lasers are aligned along the long (x) axis of the magnetic trap, and the lasers are frequency narrowed and stabilized by locking them to a home-built reference cavity that is described in detail elsewhere [26]. With this scheme we reach a linewidth $\lesssim$10 kHz for both lasers. For the Rydberg excitation we use blue and infrared powers of 90 mW and ~0.5 μW, respectively. In order to increase the two-photon Rabi frequency the coupling blue beam is focused down to a waist of 90 μm. This leads to a blue Rabi frequency at full power of $\Omega_c \sim 10$ MHz for the $5P_{3/2}$-$30S_{1/2}$ transition. The infrared beam waist at the position of the atoms is 520 μm. The detuning to the intermediate $5P_{3/2}$ state is

100 MHz towards the blue for the 780-nm laser to reduce losses due to intermediate-state scattering. Finally, after the Rydberg excitation pulse, the remaining ground-state atoms (Rydberg atoms are lost during the excitation pulse by decay into nontrapped states) are released and detected after a time of flight of several milliseconds using absorption imaging.

By scanning the blue frequency across resonance and measuring the number of remaining atoms as a function of this frequency we obtain Rydberg loss spectra. In order to change the electric field at the position of the atoms we pulse a voltage during the Rydberg excitation. This voltage is applied to one of the on-chip wires [wire 4 in Fig. 2(a)] during the magnetic-trapping and Rydberg-excitation phase. The wire we use to generate the electric field at the position of the atoms (wire 4) is 10 μm wide, and the distance of its center from the nearby edge of wire 5 is 35 μm. All the other wires (except wires 4 and 5) and the silicon substrate are kept floating. It is important to note that all the wires have a finite resistance (on the order of 10 kΩ) to each other via the silicon substrate [24]. Thus, as we apply a voltage to wire 4, most of the chip surface shifts voltage towards the voltage of wire 4. The exception is wire 5, where the voltage (and current) is pinned by the current supply attached to it. To characterize the voltage distribution across the chip surface we use the fact that the resulting voltages on most of the wires are accessible outside the vacuum system via a multipin vacuum feedthrough. We have measured these voltages under operating conditions (i.e., with current for magnetic trapping applied to wire 5 and varying the voltage on wire 4) and found that the voltage on all the wires (with the already noted exception of wire 5) shifts roughly linearly with the voltage on wire 4. These voltages were used to calculate the direction of the applied electric field (the direction of the u axis in Fig. 2). A further detail that is relevant is that we found a slight asymmetry in the measured voltages on the other wires as the sign of the voltage difference between wire 4 and the center of wire 5 changed (see Sec. III A).

A. Stark map of the *S* state

In order to calibrate the relation between the applied voltage and the locally applied electric field at the position of the atoms we first measured a Stark map of the $30S_{1/2}$ state by taking Rydberg loss spectra for various applied voltages. We set the polarization of the blue and infrared lasers to be σ_- and σ_+, respectively. We fitted a Gaussian to each Rydberg spectrum in order to obtain the amplitude, position, and FWHM of the loss feature. The resonance position and width of the Rydberg feature are plotted as a function of the applied voltage in Fig. 3. The vertical bars represent the FWHM of each feature in the spectrum. As expected, in the presence of electric field gradients (see Sec. III C), the feature gets broader as we increase the applied field. We found that the voltages on the on-chip wires are slightly asymmetric around the applied voltage on wire 4 V_{ap}. A possible explanation for this behavior is a leakage current between the chip wires that is slightly asymmetric in the voltage difference between the wires. This produces an asymmetry of the shift in frequency around $\sim$1.4 V. To account for this we fit separate quadratic functions with a shared apex to the data in order to produce a voltage-to-field relation. The quadratic functions smoothly

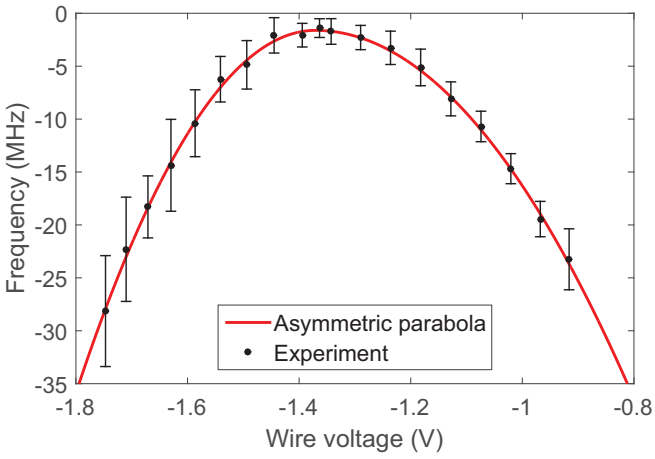

FIG. 3. Measured Stark shift and broadening for the $30S$ state. We use these measurements to calibrate the actual applied electric field we are generating at the position of the atoms. The plot shows the resonance shift of the Rydberg signal at different applied voltages. The vertical bars are the measured FWHM of each feature obtained from a Gaussian fit. We fit two quadratic functions to the data in order to obtain the parameters in Eq. (2); see the main text for details.

connect at the top but have different curvatures. The resulting fits are shown in Fig. 3. Using the known polarizability of the $30S$ state [27], we can extract a relation between the applied voltage and the field generated at the position of the atoms using

$$\Delta = -\tfrac{1}{2}\alpha_{30S}E^2, \tag{1}$$

where $\alpha_{30S} = 1.39\,\mathrm{MHz/(V/cm)^2}$ is the polarizability of the $30S$ state and Δ is the energy shift of the Rydberg feature produced by the presence of an electric field E. Using these two different fits, we obtained a field-voltage relation of the form

$$E_{ap} = c_i(V_{ap} - V_0). \tag{2}$$

Here, E_{ap} is the applied field at the position of the atoms, and c_i are two different coefficients depending on which side of the parabola the applied field is: $c_1 = 12.4\ \mathrm{cm^{-1}}$ and $c_2 = 16.4\ \mathrm{cm^{-1}}$ for $V_{ap} > -1.37$ V and $V_{ap} < -1.37$ V, respectively. $V_0 = -1.37$ V is the offset voltage we get for which the Stark shift is minimal. This voltage is consistent with the inferred voltage at the center of the trapping wire [wire 5 in Fig. 2(a)] produced by the current we send through it to generate the magnetic trap. Note that a small stray field along the direction of $\vec{E}_{ap}$ would lead to a small shift of V_0 in the Stark map. In contrast, stray fields in the other two directions (orthogonal to $\vec{E}_{ap}$) lead to a vertical energy offset $-\frac{1}{2}\alpha_{30S}(E_x^2 + E_v^2)$ in the Stark map of the S state that does not discriminate between E_x and E_v and that would require an absolute frequency reference to calibrate.

B. Stark map of the *D* state

The knowledge of the applied electric field at the position of the atoms allows us to measure a calibrated Stark map of the $28D_{5/2}$ state. To do so we set the polarization of the blue and infrared beams to be linearly polarized in such a

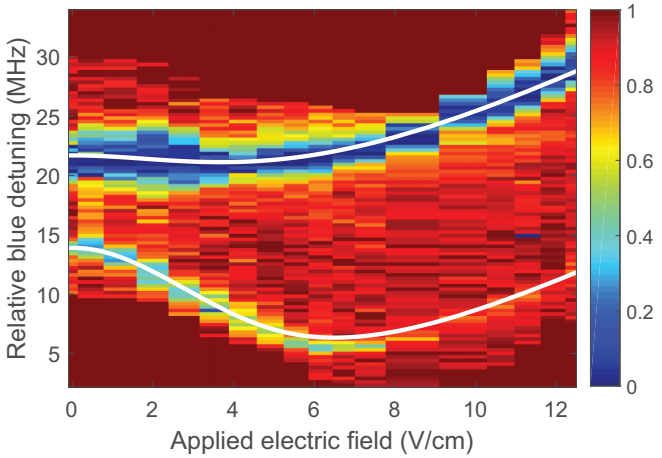

FIG. 4. The $28D_{5/2}$-state Stark map of two different sublevels: The top and bottom curves are the $m_j = 5/2$ and $m_j = 3/2$ sublevels (ZEL), respectively. The color scale indicates the normalized number of atoms, normalized to the number of atoms measured when the Rydberg excitation lasers are off resonance. The measurements were taken outside the dark red area. We deliberately saturated the upper sublevel in order to be able to see the other one, which has a much smaller coupling strength. The white lines are the resulting fitted curves for the resonance position of each sublevel where the parallel and perpendicular electric fields are used as fitting parameters (from the fit we get $E_x = 0$ V/cm and $E_v = 1.98$ V/cm, respectively; see main text for details).

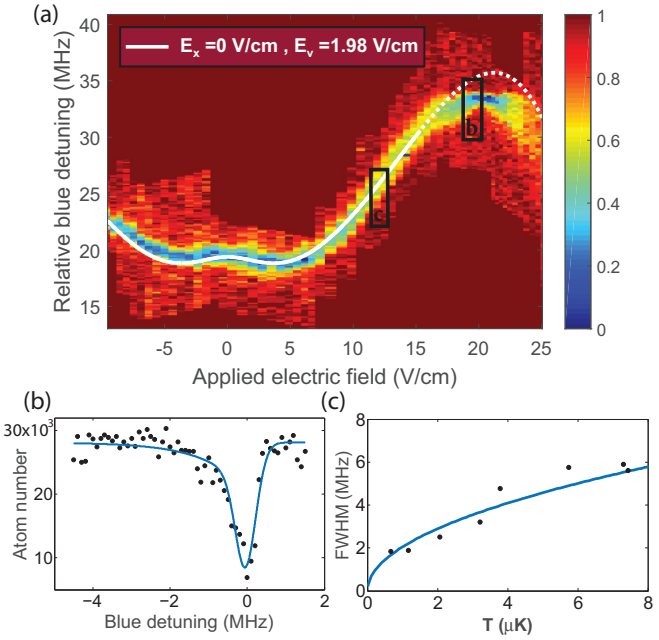

FIG. 5. Rydberg loss spectroscopy of the $28D_{5/2}$ state for different applied fields. (a) The top state in Fig. 1(a) considering the voltage-to-field conversion. The color scale indicates the normalized atom number in each spectrum; measurements are performed outside the uniform dark red area. The dashed white line shows the resulting fitted curve, obtained using only the data within the area of the solid white line (below 15 V/cm). (b) At $E_{ap} \sim 19$ V/cm the Rydberg feature is asymmetric due to the presence of field gradients. Therefore, a skewed Gaussian (solid curve) is fit to the data. A small asymmetry is observed around 0 V/cm; it is due to a slow residual drift of the cavity to which the Rydberg lasers are locked [26]. (c) The measurement of the FWHM of the loss feature at different temperatures at an applied electric field of $E_{ap} \sim 12$ V/cm where the Rydberg feature is symmetric.

way that we are able to see both the $m_j = 5/2$ and $m_j = 3/2$ states (ZEL). The resulting Stark-Zeeman map is shown in Fig. 4. We used Eq. (2) to transform the x axis from an applied voltage to an applied electric field at the position of the atoms. We fitted two Gaussians to each spectrum for a given applied field and extracted the main properties of the two features: amplitude, FWHM, and position. The comparison of the resonance position obtained from the data with the calculated ones gives us values for the components of the stray field E_x (parallel to $\vec{B}$) and E_v (perpendicular to $\vec{B}$ and $\vec{E}_{ap}$). The analysis is based on the shape and the size of the initial dips in the Stark map (for applied fields $\leqslant 10$ V/cm) which strongly depend on the stray field configuration [see Fig. 1(b)]. Considering the values obtained for the electric-field components, we can estimate to what extent the FWHM of each feature is limited by field gradients.

From the Stark-Zeeman map in Fig. 4 we already see the initial dip in the energy shift of the resonance of both states, so we can immediately set an upper limit to the field in the parallel direction of $E_x \lesssim 2$ V/cm. The coupling strength of the $m_j = 3/2$ state is much weaker than that of the $m_j = 5/2$ (ZEL), so we have to strongly saturate the latter in order to see both at the same time. The weak feature has a much more prominent dip as a function of electric field than the strong one. Therefore, the simultaneous use of the resonance positions of both states results in a more accurate analysis of the data. However, since the $m_J = 5/2$ state is strongly saturated, it is not possible to extract an accurate value for the resonance position of the Rydberg feature. In order to get a better data set for this state we set the blue and infrared beams to be σ_+ polarized, so only the transition to the $m_j = 5/2$ state (ZEL) is allowed by selection rules. Because this state has a strong coupling, it is possible to investigate its behavior also at higher electric fields without losing the signal. The resulting Stark-Zeeman map is shown in Fig. 5(a). These data are combined with the previously measured $m_J = 3/2$ state (ZEL) data and fitted to the calculated Stark-Zeeman map [Fig. 1(b)] with the residual electric fields E_x and E_v as fitting parameters. For the fit we use only data for fields $E_{ap} < 15$ V/cm, from which we obtain $E_x = 0.0 \pm 0.2$ V/cm and $E_v = 1.98 \pm 0.09$ V/cm.[1] The resulting fitted curves are shown on top of the measured Stark-Zeeman map as white lines in Figs. 4 and 5(a).

Although the resulting fitted curves show excellent agreement with both sublevels at low field values, $E_{ap} < 10$ V/cm,

[1]The stated uncertainties in the fields, ΔE_v and ΔE_x, are calculated assuming that the reduced χ^2 value of the model is 1, $\chi_r^2 = 1$. Thus, ΔE_v and ΔE_x are obtained by allowing the χ^2 value to increase by 1 from its minimum value. The more usual approach of extracting the uncertainty from the inverse covariance matrix on the basis of the curvatures at the minimum of χ^2 is not applicable because the dependence of χ^2 on E_x was found to be nonquadratic [28].

there is a discrepancy at high field values, $E_{ap} \approx 20$ V/cm [see Fig. 5(a)]. We have verified that the frequency difference between the observed bump at $E_{ap} = 20$ V/cm and the observed dip at $E_{ap} = 5$ V/cm is reproducible and not affected by slow drifts in the experimental frequency calibration. This was done by measuring the frequencies of the observed bump at $E_{ap} = 20$ V/cm and the observed dip at $E_{ap} = 5$ V/cm directly after one another and confirming their vertical spacing in Fig. 5(a). One source for a reduction in the peak frequency shift at 20 V/cm is the differential ac Stark shift of the Rydberg level as the character of the state changes with increasing applied electric field. We calculated this to give a modest contribution, a downshift in frequency of ~0.5 MHz at $E_{ap} =$ 20 V/cm. In short, the discrepancy between our calculation and the experimental results around $E_{ap} = 20$ V/cm may be due to a combination of factors and is still under investigation. This discrepancy does not affect the determination of E_x and E_v because it is visible only at high field values ($E_{ap} > 15$ V/cm), where small residual fields do not play a role.

C. Electric field gradients

We now focus on possible gradients in the electric field as a source of broadening in the experimental spectra. Already from the calculations we can conclude that in the areas where the Stark shift has an extremum as a function of field the Rydberg loss feature will become asymmetric. This is due to the quadratic character of the energy shift around the extremum and the finite size of the cloud, which means that different parts of the cloud sample different values of the electric field. Figure 5(b) shows an example of a spectrum taken at $E_{ap} = 19$ V/cm, where the effect of gradients in the Rydberg spectrum is enhanced due to the high curvature of the frequency-field relation. From this spectrum it is possible to see the asymmetry of the signal. This observed asymmetry supports the assumption that the broadening of the Rydberg feature is caused by the presence of field gradients at the position of the atoms.

The above argument implies that the Rydberg feature is symmetric in the field regime where the energy shift is linear. This linear regime is a characteristic that is unique for D states and that can actually be used to extract an approximate value of the electric field gradient in the volume of the atoms. Due to the elongated character of the cloud (along x) and the fact that the applied field is along u (see Fig. 2), the measured spectra are more sensitive to gradients related to the change in potential V in the x and u directions in Fig. 2. Thus, our measurements and calculations are dominated by the gradient, $g = \partial^2 V/\partial x \partial u$, the variation along the long direction of the cloud of the field component E_u. To extract this value from the data we assume a Gaussian density distribution along the long direction of the cloud, $n(x,T) \propto \exp[-x^2/2\sigma_x(T)^2]$, with a size set by the temperature: $\sigma_x(T) = \sqrt{k_B T/m\omega_x^2}$, where k_B is the Boltzmann constant, m is the atomic mass, and ω_x is the trap frequency in the long direction.

The cloud samples different values of the field, which are set by the gradient g and the size of the cloud via the expression $\delta E(x,g) = gx$. At the same time these fields are related to the linear shift in energy via $\Delta(x,g) = a\delta E(x,g)$, where $a =$ 1.44 MHz/(V/cm) is the slope we get when we fit a line to the part of the Stark shift of the upper state of the $28D_{5/2}$ manifold that has a linear behavior. The FWHM of the Rydberg spectrum depends on the field gradient, temperature (because it sets the size of the cloud), and the zero-field linewidth. The latter corresponds to the linewidth of the spectrum set by any other mechanism of broadening besides electric-field effects. In order to extract the gradient, we set the applied electric field to $E_{ap} \sim 12$ V/cm (where the shift is linear with the field) and vary the temperature by changing the final rf frequency in the evaporative cooling process. Finally, the FWHM of the Rydberg loss spectrum is plotted as a function of temperature; the results are shown in Fig. 5(c). We refrained from using a fitting function that includes a finite value for the FWHM at $T = 0$ K, corresponding to the previously mentioned zero-field linewidth. This is not necessary in our fit due to the lack of data points for low temperatures (limited by the signal-to-noise ratio because of the low atom number); further, it does not affect the estimate of the gradient because it is mainly set by the slope of the fitted curve. From our data we obtained a field gradient of $g = 179 \pm 9$ V/cm^2 along the long direction of the cloud. This is the value for a field gradient that explains the broadening of the Rydberg feature. In particular, it explains the increase of the FWHM for higher temperatures shown in Fig. 5(c). Interestingly, it also allows a comparison with the maximum widths observed in the S-state spectrum of Fig. 3. When the applied field dominates over the residual fields, the width of the spectrum is sensitive to the same electric field gradient we determined above. The expected FWHM width of the spectrum when the applied field dominates is then $\alpha_{30S} E_{ap} g \delta x$, with δx being the FWHM length of the cloud. This yields a FWHM of 9 MHz for a wire voltage of -1.75 V in Fig. 3, consistent with the measured width.

Another reason that might explain the difference between the model and the experimental data at low temperatures is the omission of density effects. At low temperatures there is an important increase in density which means Rydberg-mediated interactions might be playing a role in the observed width. Our model does not consider this. However, the value of the gradient is set mainly by the slope of the curve which is set by higher-temperature data ($T > 2\,\mu$K). In this area, the dominant mechanism of broadening is the effect of gradients, particularly along the long direction of the cloud. The investigation of Rydberg-mediated interactions and collective effects at lower temperatures and higher densities is the subject of further work and is beyond the scope of the present paper.

IV. CONCLUSIONS AND OUTLOOK

We characterized the vector components of the stray electric field close to the chip surface in our atom-chip experiment by comparing calculated S and D Stark-Zeeman maps with experimental data. We applied a voltage to one of the on-chip wires in order to generate a field at the position of the atoms. The field is characterized using a measured S-state Stark-Zeeman map, which is then used as a tool to calibrate the field axis of the D-state Stark-Zeeman map. The energy shift of D states when applying an electric field is nontrivial and has an initial dip in energy. The minimum of this dip, and therefore the change in curvature, strongly depends on the values of stray electric fields along different directions. The

values of these field components are obtained by fitting the data to the simulated Stark-Zeeman map. We obtained values for the residual fields that are relatively small, namely, $E_x = 0.0 \pm 0.2$ V/cm and $E_v = 1.98 \pm 0.09$ V/cm. We attribute this observed residual field mainly to stray fields produced by rubidium adsorbates on the surface of the chip. In fact, the total stray field is about a factor of 2 lower than that observed at the same distance (100 μm) under similar conditions using electromagnetically induced transparency [10], where the field was attributed to rubidium adsorbates on the gold surface. The lower value we observe may be due to the somewhat elevated temperature of the current-carrying gold wire in our system, which should lead to reduced Rb coverage. Another contribution to the electric field comes from the current-carrying wire. Within the wire the electric field is given by the current and the resistivity of the gold wire and is $\sim$1 V/cm along the wire (in the x direction). At the position of the atoms we calculate this to lead to a contribution of $\sim$0.4 V/cm along the x direction. Since from the $28D$-state spectra we find $E_x = 0$ V/cm, this field is apparently compensated by other contributions to the residual field (likely the Rb adsorbates).

We also made use of the linear response of D states to applied electric fields. In this region the Rydberg signal is symmetric, and the increase in linewidth as we increase the size of the cloud is related to the field gradient at the position of the atoms. The value of the gradient allows us to set a lower limit for the linewidth of the Rydberg signal, setting the stage for future research of Rydberg-mediated interactions in our setup.

On the one hand, the elongated character of our cloud sets a limit for the linewidth we can observe due to different parts of the cloud sampling different fields, but on the other hand, it has been demonstrated that the one-dimensional character has advantages when observing Rydberg-mediated interactions [29]. From this research we can conclude that atom-chip experiments are a promising tool for the study of Rydberg systems. The level of on-chip control over the electric fields demonstrated here is promising for the observation of Rydberg blockade and Rydberg-mediated interactions in ultracold gases trapped on a chip, which is relevant for quantum information science and technology in integrated and compact systems. The next generation of chips is being designed in which the stray electric fields along E_x and E_v can be compensated using electrodes placed as an extra layer on top of the chip. The characterization of the fields in the new setup will be done using the electrometry process described in this paper.

ACKNOWLEDGMENTS

This work was financially supported by the Foundation for Fundamental Research on Matter (FOM), which is part of the Netherlands Organisation for Scientific Research (NWO). We also acknowledge financial support by the EU H2020 FET Proactive project RySQ (640378).

[1] T. F. Gallagher, *Rydberg Atoms* (Cambridge University Press, Cambridge, 2005).
[2] S. Haroche, Rev. Mod. Phys. **85**, 1083 (2013).
[3] M. Müller, L. Liang, I. Lesanovsky, and P. Zoller, New J. Phys. **10**, 093009 (2008).
[4] M. Saffman, T. G. Walker, and K. Mølmer, Rev. Mod. Phys. **82**, 2313 (2010).
[5] H. Gorniaczyk, C. Tresp, J. Schmidt, H. Fedder, and S. Hofferberth, Phys. Rev. Lett. **113**, 053601 (2014).
[6] D. Tiarks, S. Baur, K. Schneider, S. Dürr, and G. Rempe, Phys. Rev. Lett. **113**, 053602 (2014).
[7] J. Reichel and V. Vuletic, *Atom Chips* (Wiley, Weinheim, 2011).
[8] R. P. Abel, C. Carr, U. Krohn, and C. S. Adams, Phys. Rev. A **84**, 023408 (2011).
[9] C. Hermann-Avigliano, R. C. Teixeira, T. L. Nguyen, T. Cantat-Moltrecht, G. Nogues, I. Dotsenko, S. Gleyzes, J. M. Raimond, S. Haroche, and M. Brune, Phys. Rev. A **90**, 040502(R) (2014).
[10] A. Tauschinsky, R. M. T. Thijssen, S. Whitlock, H. B. van Linden van den Heuvell, and R. J. C. Spreeuw, Phys. Rev. A **81**, 063411 (2010).
[11] H. Hattermann, M. Mack, F. Karlewski, F. Jessen, D. Cano, and J. Fortágh, Phys. Rev. A **86**, 022511 (2012).
[12] J. A. Sedlacek, E. Kim, S. T. Rittenhouse, P. F. Weck, H. R. Sadeghpour, and J. P. Shaffer, Phys. Rev. Lett. **116**, 133201 (2016).
[13] S. Weber, C. Tresp, H. Menke, A. Urvoy, O. Firstenberg, H. P. Büchler, and S. Hofferberth, J. Phys. B: At. Mol. Opt. Phys. **50**, 133001 (2017).
[14] N. Šibalić, J. Pritchard, C. Adams, and K. Weatherill, arXiv:1612.05529.
[15] M. Mack, F. Karlewski, H. Hattermann, S. Höckh, F. Jessen, D. Cano, and J. Fortágh, Phys. Rev. A **83**, 052515 (2011).
[16] W. Li, I. Mourachko, M. W. Noel, and T. F. Gallagher, Phys. Rev. A **67**, 052502 (2003).
[17] J. Han, Y. Jamil, D. V. L. Norum, P. J. Tanner, and T. F. Gallagher, Phys. Rev. A **74**, 054502 (2006).
[18] K. Afrousheh, P. Bohlouli-Zanjani, J. A. Petrus, and J. D. D. Martin, Phys. Rev. A **74**, 062712 (2006).
[19] B. Numerov, Mon. Not. R. Astron. Soc. **84**, 592 (1924).
[20] B. Numerov, Astron. Nachr. **230**, 359 (1927).
[21] M. L. Zimmerman, M. G. Littman, M. M. Kash, and D. Kleppner, Phys. Rev. A **20**, 2251 (1979).
[22] D. Martin, Proc. Edinburgh Math. Soc., Ser. 2 **12**, 67 (1960).
[23] A. H. van Amerongen, Ph.D. thesis, University of Amsterdam, 2008.
[24] J. Van Es, P. Wicke, A. Van Amerongen, C. Rétif, S. Whitlock, and N. Van Druten, J. Phys. B **43**, 155002 (2010).
[25] A. H. van Amerongen, J. J. P. van Es, P. Wicke, K. V. Kheruntsyan, and N. J. van Druten, Phys. Rev. Lett. **100**, 090402 (2008).
[26] J. de Hond, N. Cisternas, G. Lochead, and N. J. van Druten, Appl. Opt. **56**, 5436 (2017).
[27] M. S. O'Sullivan and B. P. Stoicheff, Phys. Rev. A **33**, 1640 (1986).
[28] W. H. Press, B. P. Flannery, S. A. Teukolsky, W. T. Vetterling, and P. B. Kramer, *Numerical Recipes: The Art of Scientific Computing* (Cambridge University Press, Cambridge, 1987).
[29] M. Płodzień, G. Lochead, J. de Hond, N. J. van Druten, and S. Kokkelmans, Phys. Rev. A **95**, 043606 (2017).